Usage Report for Fiscal Year 2019

Project Title:

Computational Studies of Muon Locations, Electronic Structures and Electron Transport in High-T_c Superconductor, Organic, Organometallic and Biological Systems.

Name:

○Shukri Sulaiman (1,2), Mohamed Ismail Mohamed-Ibrahim (1,2), Isao Watanabe (2), Dita Puspita Sari (2,3), Muhammad Redo Ramadhan (2,4), Irwan Ramli (2,5), Wan Nurfadhilah Zaharim (1,2), Sawasdee Tanawat (2,6), Peter Greimel (2)

Laboratory at RIKEN:

(1) Universiti Sains Malaysia, Malaysia
(2) RIKEN, Nishina Center, Japan
(3) Shibaura Institute of Technology, Japan
(4) Universitas Indonesia, Indonesia
(5) Universitas Cokroaminoto Palopo, Indonesia
(6) Suranaree University of Technology, Thailand

1. Background and purpose of the project, relationship of the project with other projects

μSR spectroscopy is one of the techniques that are capable of providing information at such microscopic properties due to high sensitivity to local magnetic and electronic environments. The knowledge of various phenomena such as magnetism, hyperfine interactions, and electron transport can be obtained. μSR spectroscopy commonly uses positively charged anti-muon (μ+), as a dilute magnetic probe.

μSR experiments provide a measure of the microscopic field distribution at the interstitial sites where the muon stops inside the sample. Hence, the muon stopping sites is crucial to determining electronic properties, for instance, long-range magnetic ordering or localized magnetic moments. μSR spectroscopy, however, has a limitation on the determination of possible muon location. This limitation, however, can be addressed using the density functional theory (DFT) approach, which is also used as a valuable strategy to aid the interpretation of μSR experimental data., This is because the comparison of the information on the muon stopping sites between the computational and μSR data can ultimately provide a more accurate and better understanding of the electronic structures for both pure and muonated systems of each target material.

There are six different target materials that have been studied in this project. The background study and characteristics of each target material are elucidated separately as below:

i. Organic magnets

In this project, there are two series of organic magnets material have been studied which are β'-X[Pd(dmit)$_2$]$_2$ [X = EtnMe$_{4-n}$(P, Sb)] and κ-(BEDT-TTF)$_2$Cu[N(CN)$_2$]X X = Cl, Br. Both of the systems share some general properties, for instance, both are classified as two-dimensional systems and their physical properties are determined by the molecular orbital overlap. In addition, they also exhibit various types of behaviours including superconducting, magnetic and Mott insulating.

Both types of materials, however, are different in terms of their structure in which β'-X[Pd(dmit)$_2$]$_2$ [X = EtnMe$_{4-n}$(P, Sb)] system possess column structure and planar Fermi surface while the other series have

non-columnar structures and non-planar Fermi surface. In addition, it is obvious that the conducting part in which the unpaired spin located in the materials are different. For ß'-X[Pd(dmit)$_2$]$_2$, the electron is delocalized throughout the anion, whereas for κ-(BEDT-TTF)$_2$Cu[N(CN)$_2$]X the electron is delocalized throughout the cation. The delocalization behaviours of the unpaired electron in both organic magnets are responsible for the magnetic characterization of the systems.

a. *β′*-X[Pd(dmit)$_2$]$_2$ X=EtnMe$_{4-n}$(P, Sb)

β′-X[Pd(dmit)$_2$]$_2$ where X is the cation, is an important class of ion radical salts that have many potential applications, especially in spintronics. The exploitation of their properties requires a thorough understanding of their electronic and magnetic properties at the microscopic level, particularly the magnetic ground state and the structure of their long-range magnetic ordering. The unit cell and structural characteristics are shown in Fig. 1.

Several experimental investigations concluded that these systems are Mott insulators with antiferromagnetic (AF) ordering, where a spin -½ localized on each dimer. Of these reports, one μSR measurement has revealed a long-range AF ordering with TN = 39.3 K in *β′*-Me$_4$P[Pd(dmit)$_2$]$_2$ compound. In the experiment, three signals were detected, which were presumed to be at the inequivalent sulfur atoms, consisting of thiol, thiolate, and thione moieties, as depicted in Fig. 2. One of the uncertainties in the experiment is that one does not know the exact location of the muon, i.e. the exact place in the host materials where the field is measured. Therefore, it requires a further investigation that can be accomplished using appropriate computational techniques, which has been the motivation of the work presented here.

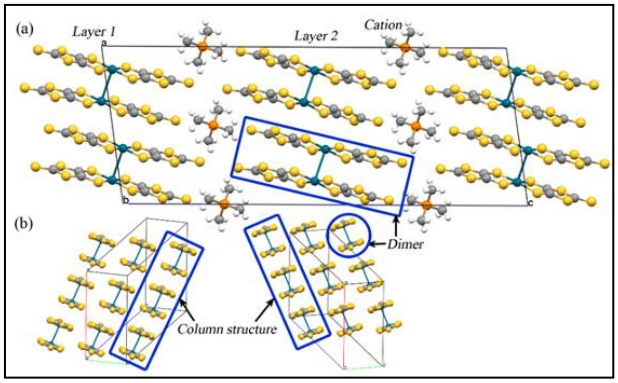

Fig. 1. (a) Unit cell of *β′*-Me$_4$P[Pd(dmit)$_2$]$_2$. (b) Solid-crossing column structure of *β′*-Me$_4$P[Pd(dmit)$_2$]$_2$.

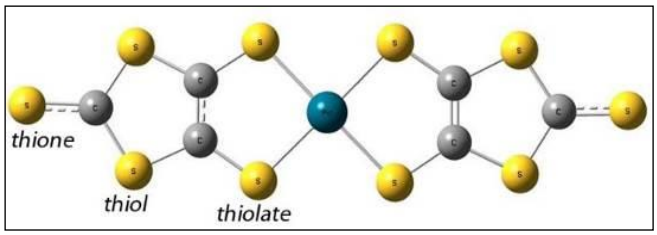

Fig. 2. Three inequivalent sulfur sites, consisting of thione, thiol, and thiolate.

b. *κ*-(BEDT-TTF)$_2$Cu[N(CN)$_2$]Cl and *κ*-d8-(BEDT-TTF)$_2$Cu[N(CN)$_2$]Br

κ-(BEDT-TTF)$_2$Cu[N(CN)$_2$]X (X=Cl, Br, and I) which also abbreviated as κ-ET is a part of charge-transfer salts materials. There are two ET layers in one unit cell, which are layer A and layer B. In one layer, they consist of two inequivalent ET dimers with ½ holes per dimer and various monovalent anions, X as can be seen in Fig. 3 below. The conducting ET dimers are located on the corners and centers of a rectangular lattice. The orientation between both dimers on the corners and centers are different with the angle nearly 90°. The dimers donate one of the electrons to the anion, hence leave one hole behind. The hole in the dimer results in a half-filled electronic band, which is very crucial for the requirement of the Mott-insulating state. On the other hand, the cross-section of the Fermi surface is equal to the first Brillouin zone.

The cation layer lies in the ac-plane while the anion layer is a long polymeric chain extended along a direction. The anion part forms a closed shell and

does not responsible for electronic conduction and magnetism. Due to the simplicity of the electronic properties of this compound, it can provide knowledge on basic characteristics such as magnetism, superconductivity and electronic band formation by application of chemical and hydrostatic pressures.

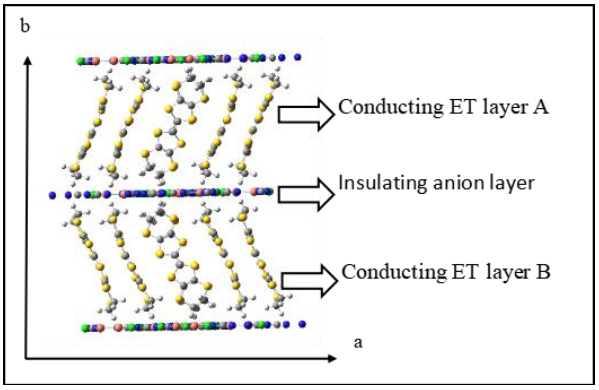

Fig. 3. Insulating and conducting layer of κ-(BEDT-TTF)$_2$Cu[N(CN)$_2$]X, with ET=-(BEDT-TTF)$_2$.

ii. Organic superconductors, λ-(STF)$_2$FeCl$_4$

The magnetism in the field-induced superconductor λ-(BETS)2FeCl4 has been intriguing and still an open debate. This organic layered magnet hosts a -d interacting spin system between BETS -spin in the conducting layer and 3*d* Fe magnetic ion in the insulating layer. In the zero-field condition the system exhibit metal-insulator transition in conjunction with the AF ordering at ~8K. It is unclear whether *p*- or *d*-spin is the driving force of the AF ordering. The idea of a simultaneous *p*- and *d*-spin ordering has also been proposed. In order to focused on the AF ordered state, we studied the sister compound λ-(STF)$_2$FeCl$_4$ which is located at the lower-pressure regime in the temperature-pressure phase diagram. The number of Se atom in λ-(STF)$_2$FeCl$_4$ is less than that of λ-(BETS)$_2$FeCl$_4$ and the AF ordering at 16K was reported from ^{1}H NMR, magnetization, and Fe Mossbauer spectroscopy. We carried out μSR measurement in λ-(STF)$_2$FeCl$_4$ and obtain the evidence of magnetic long-range ordered from muon-spin precession with two distinct muon sites. In conjunction with this experimental result, we carried out DFT calculation for the electronic minimum potential. We found two possible muon stopping sites. One is located near the Fe atom and the other is located near to hydrogen atom at the edge of STF molecule.

iii. High-Tc superconducting oxides

a. $YBa_2Cu_3O_6$

$YBa_2Cu_3O_6$ (YBCO) is a typical strongly correlated system. It shows long-range AF ordering which is suppressed by oxygen doping ($YBa_2Cu_3O_{6+x}$) and superconductivity appear at x ~ 0.4. The detail study of long-range AF is one of the key to understand how the superconductivity in this system appear. The μSR experiment has great contribution to reveal the magnetic properties of this system. The unknown positions of the implanted muon in this system prevent us to obtain a deeper understanding.

We tackle this problem by using DFT calculation. Since YBCO is a strong correlation system, we need to include Hubbard parameter, U. The U has played an important role to localize electron and establish spin. We have successfully determined three different muon-site in YBCO which consistent with our high statistic μSR experimental data.

The internal field at each muon site can be directly extracted from the experimental data. Thus, we need to validate those internal fields by calculating the internal fields at each muon site which has been estimate from DFT calculation. The internal field calculations need to take into account the zero-point vibration energy of muon, the muon's perturbation of the system and the effect of the U value.

b. $La_{2-x}Sr_xCuO_4$

La_2CuO_4 (LCO) is the parent compound for the Cuprate-based, high-T_C superconducting material. This system is known to have an AF insulating behavior and classified as the Mott-insulator. One accurate experiment to prove the existence of this AF

behavior is the μSR technique. In this technique, the implanted muon which sensed magnetic field will precess due to the Larmor precession. One of the first studies on LCO, shows that the precession frequency is at 5.5 MHz, using the muon's gyromagnetic ratio (γ_μ = 135.538817 MHz/T). The Internal field that was felt by muon in the LCO system was determined to be around 410 G. Our latest μSR experiment on single crystal LCO shows that there are 3 sources of internal field, meaning that there are 3 possible unique muon positions. While clear precessions have been observed, the exact location of the implanted muon is still unclear, hindering the ability of μSR technique to reveal more information about the cuprates system.

We utilize large supercell structure containing 32-unit cells inside with the formation of 4 × 4 × 2, with the single hydrogen atom to simulate the implanted muon. By observing the electrostatic potential of the supercell system, we observe that there are indeed 3 possible muon positions labelled as M1, M2, and M3. By considering the local effect of each implanted muon position and the zero-point vibration motion for each muon we calculate the internal field on each position and compared with the experimental results. Even with using this method, we still observe slight differences between the calculated internal field, and the experimental field. In this project we tried to observe the possible reasons for these slight differences.

As the project for the LCO system has already reaching to its final phase, we plan to extend our method to the doped-phase of the cuprate system. In this fiscal year, we just simply calculate the 12.5% Sr-doped case to obtain correct electronic ground-state for this system as the initial test. Before extending it to the detailed calculation on the next fiscal year.

iv. Single strand synthetic DNA model molecules

Electron transport occurs in many important biological processes such as storage and consumption of energy, enzyme response, and DNA UV damage repair. μSR is an experimental technique that can be used to study electron transport phenomena in DNA at the microscopic level. The changes in the electron transport properties due to damages in DNA can be probed by using muon hyperfine interactions which are very sensitive to the changes in the electronic structure surrounding the muonium (Mu) trapping sites.

To systematically study the effect of damages on DNA to the behavior of electrons, it is, therefore, crucial to develop baseline data using DNA systems with known DNA sequences. In previous project, the Mu hyperfine interactions at all possible Mu trapping sites in the four nucleobases and four nucleotides were investigated. The results show that the presence of a methyl group or a sugar phosphate group to the nucleic acid bases has a direct effect on the electronic structure of the system. In this FY2019, the distortion test in the geometry of guanine nucleobase when Mu is added to the possible trapping sites was conducted. An analysis on the optimized muoniated systems structure was done to investigate whether the presence of Mu caused the guanine base ring to deviate from the planar shape.

In real, DNA consists of two polynucleotide chains twisted around each other in the form of a double helix. Each nucleotide units consist of nitrogenous bases ans sugar phosphate backbone. The existence of sugar phosphate backbone and neighbouring bases can give effect to the electronic structure of the system. Accordingly, this calculation was extend using bigger cluster size with more bases so that the effect of neighbouring bases could be included. 12mer single strand DNA with homogeneous nitrogenous bases was chosen as a model of this study.

v. Thiolated gold nanoclusters, [$Au_{25}SR_{18}$]

Thiolate protected Au nanoclusters have recently attracted significant research interest due to their fundamental physics as well as practical

applications in the nanocluster technology. Recent advances in controlled syntheses show that the exact number of core atoms and ligands of very small metal nanoparticles can be regulated, referred to as "clusters". Bulk gold is known to be extremely inert. Encapsulated thiolate gold nanoclusters, on the other hand, exhibit very distinct features, where a tiny but significant magnetic moment seems to appear, thus making them as the potential materials for high-density memory devices, spintronics, quantum computing, and opto-magnetic devices.

These nanoclusters display interesting optical properties such as intense photoluminescence, which arises from discrete electronic energy level transitions attributed to the strong quantum confinement effects, induced by the ultra-small space occupied by the gold atoms (<2 nm). These properties have made the clusters different than the metal nanoparticles or even their bulk metals. Therefore, due to this reason, it is considered that the fractionated gold nanoclusters are molecular in nature. These nanocluster materials clearly demonstrate how the fundamentals of quantum mechanics play their role in determining not only the discrete nature of the electronic states but also the quantum of separation between the energy levels.

Typical gold nanoclusters may contain from 12 to 250 Au atoms with 144 being the size that borders between bulk and nanocluster in relation to the distinction in properties. Au25 is considered the optimum size to exhibit magnetism due to the odd number of electrons that leads to an unpaired spin in the system. Fig. 4 shows the structural characteristics and labelling of the components of $[Au_{25}(SR)_{18}]^0$ cluster with R = hexyl.

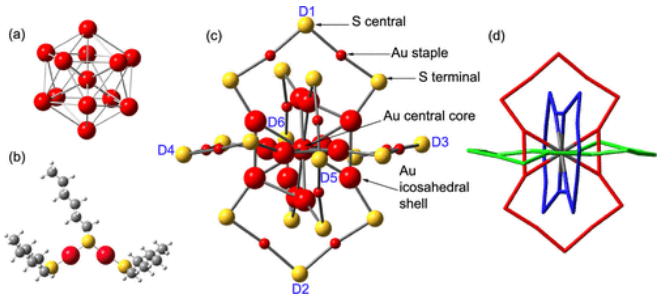

Fig. 4: (a) Structure of the inorganic Au core and semi-rings that form the $[Au_{25}(SR)_{18}]^0$ cluster with R = hexyl. (a) Au13 core, (b) dimeric staple motif, (c) Encapsulation of Au13 by the six staple motifs (hexyl groups are not shown), (d) interlocked Au8S6 rings (Legend: red = Au; yellow = S).

The reports on the magnetic properties of thiolate protected gold nanoclusters $Au_{25}SR_{18}$, however, are conflicting, where different magnetism has been concluded for the nature of the cluster, and hence, has become the motivation for our studies. The main objective of this research is to study the electronic and magnetic properties by implementing the muon technique using DFT cluster method, hoping that it can serve as a useful insight, particularly in the magnetism studies.

2. Specific usage status of the system and calculation method

There are two main ab initio quantum mechanical programs have been utilized in this group, namely, Gaussian16 and Vienna Ab initio Simulation Package (VASP) software. The Gaussian program package employs the linear combination of atomic orbital molecular orbital (LCAO-MO) technique, which is more suitable for the electronic structure studies of molecular systems. The VASP software, on the other hand, employs pseudopotentials or the projector-augmented wave method and a plane wave basis set, which has been used in the band theory calculations for solid systems. In addition, the ADF software has also been used in our computational work since it is known to provide better results on the hyperfine coupling constant (HFCC).

For FY 2019 project, there is a total of six users have been approved for the core hours. To date, only the BWMPC resource unit has almost reached the approved limit of consumption with 81% of usage. The GWMPC resource unit, on the other hand, shows a very low percentage of consumption, being only about 14%. One of the reasons is that the sizes

of some target systems are enormous, hence the calculations cannot be performed using this resource unit. Second, three users have withdrawn themselves from this project earlier due to retirement (username = mael08) and one of them with the username of suju717, have finished her studies. The results obtained from the calculations by using all the resource units prove that the HOKUSAI Great Wave supercomputer facility is crucial and extremely useful for our group research, particularly for the large-scale calculations.

3. Result

A considerable amount of computational effort has been done in FY2019 on the different systems, described in section 1. The data form the computational studies is accumulated to assist the interpretation of μSR experiments. The results for each subproject are reported separately and are as follows:

i. Organic magnets

The implementation of these organic systems has been partitioned into two subprojects, which is for: (a) β'-X[Pd(dmit)$_2$]$_2$, and (b) (BEDT-TTF)$_2$X systems. The results for each system are presented separately as follows:

a. β'-X[Pd(dmit)$_2$]$_2$ X=EtnMe$_{4-n}$(P, Sb)

We have successfully determined the electronic structure of β'-X[Pd(dmit)$_2$]$_2$ X=EtnMe$_{4-n}$(P, Sb) by employing the DFT cluster method. The results have been recently published in the journal of Materials Science Forum. For reference, please see attached our publication entitled "Effects of Polarization Function on the Spin Contamination and Distribution in β'-EtnMe$_{4-n}$Z[Pd(dmit)$_2$]$_2$". This paper focuses on the effect of polarization function on the spin contamination and distribution in β'-Me$_4$P[Pd(dmit)$_2$]$_2$. From the results, it was found that the inclusion of polarization function in the calculations has resulted in the shifting of spin density from the sulfur atoms to the central Pd atoms. The [Pd(dmit)$_2$]$_2$ − dimer showing the labelling of the "dmit" groups in the one-fragment system is shown in Fig. 5. We have found a peculiar inhomogeneity in the spin distribution among the "dmit" groups in one formula unit. Its distribution, however, is significantly different in the absence of the cation moiety. Fig. 6 demonstrate the schematic views showing the inhomogeneous spin density distribution in the (a) one-fragment cluster (from our calculations), and (b) dimer cluster without the cation moiety (reproduced from Tsumuraya et al.); leading to the existence of the electron-rich and electron-poor regions in the dimer. All calculations for this present work were performed using the ONIOM method.

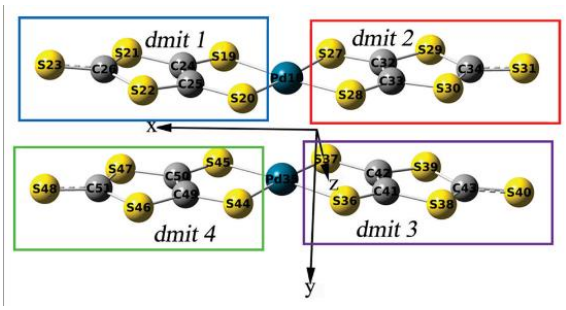

Fig. 5. [Pd(dmit)$_2$]$_2$ − dimer showing the labelling scheme for the dmit groups and individual atoms. The rectangle represents the region for each dmit group.

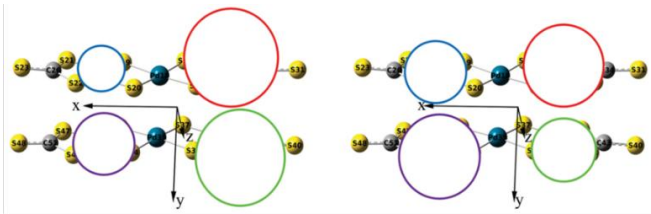

Fig. 6. Schematic views showing the inhomogeneous spin density distribution in the (a) one-fragment cluster (from our calculations), and (b) dimer cluster without the cation moiety (reproduced from Tsumuraya et al.); leading to the existence of the electron-rich and electron-poor regions in the dimer. The size of the circles implies the concentration of the electron densities, whereas the different colors of

the circles represent the region for each dmit group.

Turning next to the trapping sites for muon, the relative energies of the muon sites near the three inequivalent sulfurs in the cluster. For this case, the host cluster used is the three-fragment-cluster of β'-$Me_4P[Pd(dmit)_2]_2$ system in the AFM state are presented in Table 1. The relative energy is calculated by taking the total energy for muon at Site 1 which is near the thiolate as the reference level. Therefore, the relative energies are calculated by deducting the total energy for Site 1 from the total energy of the site of interest. From the tabulated values of relative energy in Table 1, we find that the most stable site is for muon near the thiolate. The next stable site is Site 2 corresponding to muon near the thione. The results of corresponding hyperfine interactions for both experiments and calculations show the same order of magnitude except for the muon site near thiol, where the calculated HFCC is lower by the factor of 20 than that of the experiment.

Table 1: Relative energy of the three muon sites and the corresponding hyperfine interactions from the calculations as well as μSR experiment (taken from Ohira et al., 2004).

Muon site	Total energy (eV)	Relative Energy (eV)	Calc. HFCC (G)	μSR Internal Field (G)
Site 1 (Thiolate)	-1534600.69	0.00	20.86	33.1
Site 2 (Thione)	-1534600.40	0.29	34.06	78.8
Site 3 (Thiol)	-1534598.85	1.84	0.95	26.9

b. κ-$(BEDT\text{-}TTF)_2Cu[N(CN)_2]Cl$ and
κ-d8-$(BEDT\text{-}TTF)_2Cu[N(CN)_2]Br$

For the last fiscal year, the results of DFT calculations on the muonated κ-Cl have been reported. As for this fiscal year, we will report the results on the muonated κ-d8-Br. There are four inequivalent possible muon positions in this study; S14, S17, C5 and C20. S17 is an outer sulphur atom while S14 is an inner sulphur atom. C20 and C5 are C = C inside the rings and at the center of the monomer, respectively. The relative energies of muonated κ-d8-Br with respect to the C5 position are tabulated in Table 2. As can be seen from the table, the energy is the lowest at S17 position which can consider as the most stable site.

Table 2: Relative energy of muonated κ-d8-Br with respect to the C5 position.

	Relative energy (eV)	
	B3LYP	O3LYP
S17	-0.022	-0.018
S14	0.000	0.000
C5	0.026	0.023
C20	0.030	0.028

The μSR experiment observed two signals of internal fields with the values of 37.1 G and 18.9 G. Meanwhile, there are four possible muon sites are determined from DFT calculations. The values of the HFCC (Gauss) for S17, S14, C5 and C20 are presented in Table 3 below. From the values of muon HFCC shown, the values of HFCC computed using ADF software at the B3LYP level of theory for S17 and S14 are the closest to the observation from the experiment. The values at C5 and C20 using Gaussian software also are nearest to the one from the experiment.

Table 3: Values of the HFCC (Gauss) for C5, C20, S14 and S17.

Muon site	Gaussian		ADF	
	B3LYP	O3LYP	B3LYP	O3LYP
S17	1.12	1.22	22.28	8.02
S14	1.36	1.28	16.16	9.17
C5	15.99	12.32	59.87	69.72
C20	18.73	16.62	96.93	85.50

ii. Organic superconductors, λ-$(STF)_2FeCl_4$

From the μSR measurement we obtained the information of the temperature dependence internal field in λ-$(STF)_2FeCl_4$ deduced from two kinds of frequency of muon-spin precession. The fast and slow frequencies related to the internal field of ~1800 G and ~200 G at T0, respectively. We aim to reveal the spin structure of the λ-$(STF)_2FeCl_4$ by performing DFT and dipole field calculations. After obtaining the information of the calculation of the electronic minimum potential, we confirmed the possible two muon stopping sites. Next step is to obtain the localized spin in the $FeCl_4$ and in the STF dimer in order to get the AF ground state.

The result of the localization spin calculation in λ-$(STF)_2FeCl_4$ without including the muons is shown in Fig. 7. Although the resulting spin structure shows an AF ordering the absolute value of localized magnetic moment of the spin in the STF dimer is 0.004 B which is much smaller as compared with a typical dimer Mott whose magnetic moment is ~0.1 B. The Hokusai user has done several discussions with μSR experiment and DFT calculation experts in organic antiferromagnet. The λ-$(STF)_2FeCl_4$ has some distortion in the crystal structure regarding the Se atom position making the calculation difficult.

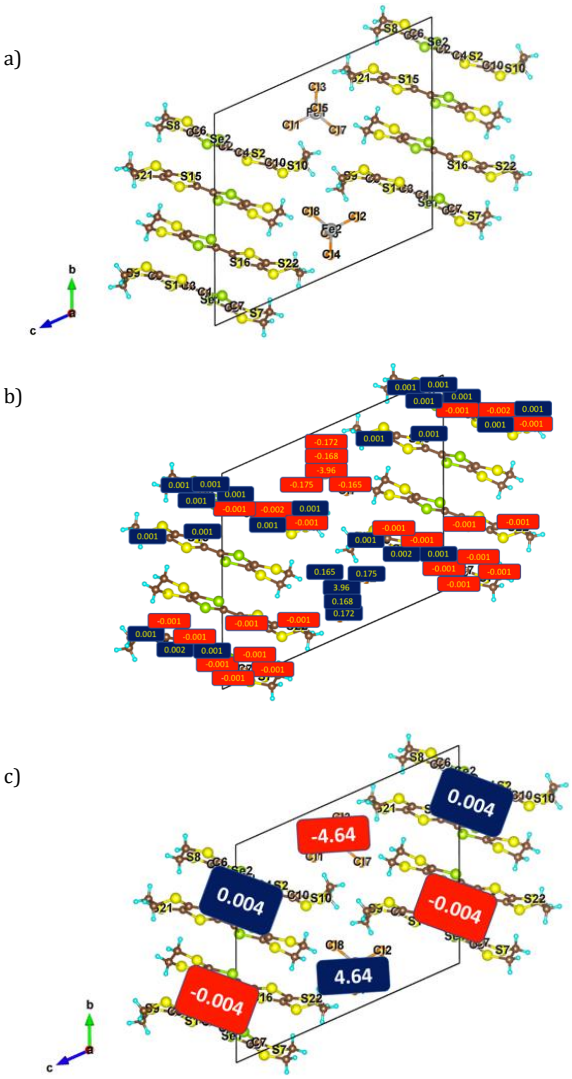

Fig. 7. Result on the spin-localization in λ-$(STF)_2FeCl_4$ without including the muons. (a) crystal structure of λ-$(STF)_2FeCl_4$ with the indicated number of atoms which has a magnetization in the z-component. (b) the absolute value of the magnetization in the indicated atoms in the unit of B. (c) the localization of magnetization obtained from the summation of the magnetization of the related atoms.

iii. High-Tc superconducting oxides

a. $YBa_2Cu_3O_6$

The muon sites in YBCO are determined by searching the local minimum potential where muon can be trapped since muon has positive charge. The DFT+U calculation results gave three different muon sites as marked M1, M2, and M3 in the Fig. 8. The previous results show that the point dipole model is overestimated the internal fields from the

experiment. We consider the covalency effect which arises from the strong hybridization between the Cu 3d and the O 2*p* orbitals and cause the extended spin in the real space. The DFT+U can provide the spin density inside YBCO. The spin density and internal fields has strong dependence on the U value. Careful tuning of the U value was required. The differences between the calculated and experimental values of the internal fields are shown as functions of the U value in Fig. 9. We determined U value to be 6.7 eV which has small different of internal field between experimental and theoretical.

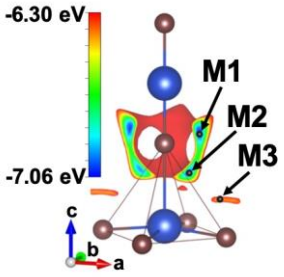

Fig. 8. Muon position in the YBCO.

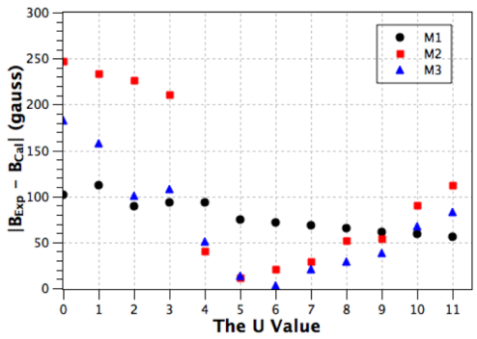

Fig. 9. Difference between the calculated and experimental values of the internal fields as functions of the U value.

b. $La_{2-x}Sr_xCuO_4$

On the previous usage report, we have already shown three possible muon positions labelled M1, M2 and M3. Fig. 10 describes the distribution of the spin density at Cu and O atomic sites in the CuO6 octahedra for both unperturbed and perturbed LCO. In the unperturbed LCO, 0.61 μB/Cu-spin is observed. Due to its AF alignment with the neighboring octahedra, the extended spin density at the O sites shows zero net magnetic moment value. In the perturbed LCO, the implanted muon causes a slight deformation on the Cu-spin density, reducing the value to 0.58 μB/Cu-spin, resulting in imbalance between neighboring Cu-atom and the finite magnetic moment value at the O-sites is observed. All of these changes are observed locally, where the local deformation effect is minimizing with the increasing size of supercell structure, making a large supercell calculation is necessity for our method to be applied.

Combining the distributed-spin model shown on Fig. 10, also the zero-point vibration motion for each muon position, we obtain the calculated internal field 409 G for the M1 position, 74 G for the M2 position, and 1320 G for the M3 position. These values are obtained using DFT+U formalism with the U-value, 7.2 eV. In comparison with the internal field that we obtain experimentally, 426 G, 109 G, and 1245 G, we realize that M1, and M3 position has high accuracy with less than 5 % differences. While M2 position has 32 % differences which is larger. Note that without taking into account distributed-spin model, the calculated internal field values are largely overestimated.

Using the VASP 5.4.4 package, we calculate the hyperfine coupling parameter on each position and found out that the hyperfine coupling contribution is less than 1 G, meaning that the differences is very unlikely to came from the hyperfine coupling parameter. Expanding Wannier wavefunction to obtain direct insight of covalent bonding nature between Cu and O atom is currently not possible to be applied to the non-collinear DFT calculation using VASP 5.4.4. package. However, the description of the extended spin density at the O sites as shown on Fig. 8, and its large effect to the accuracy of the calculated internal field gave us an indirect confirmation that the covalency effect is indeed captured via the combined studies between μSR and DFT.

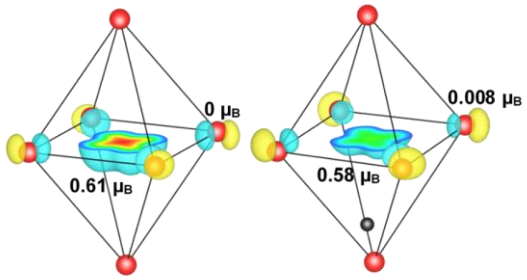

Fig. 10. Distributed-spin model for the unperturbed and M1 perturbed LCO

For the next target of Sr-doped case, we use unit-cell of tetragonal LCO, where we substitute one of the La atom with Sr atom. As the unit-cell has 8 atoms of La, 12.5% Sr-doped condition is achieved. Fig. 11 shows the difference of the density of states between non-doped and the Sr-doped case. As expected from the Sr-doped system, metallic transition is observed where the electronic states cross over the Fermi level of the system. Detailed calculation over different concentration of Sr is required in order to have a detailed discussion about the characteristic of the cuprate on this system.

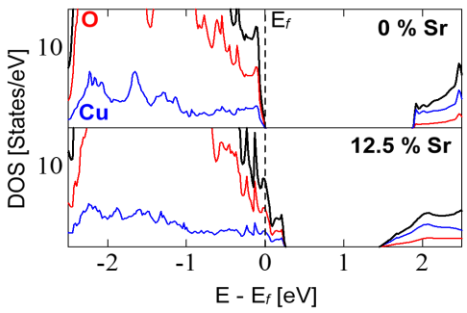

Fig. 11. Density of state (DOS) of non-doped and 12.5 % Sr-doped case of LCO.

iv. Single strand synthetic DNA model molecules

The electronic structure and the Mu hyperfine interactions in guanine nucleobase were investigated using the unrestricted Hartree-Fock cluster procedure in combination with the 6-311G(d,p) basis set. The effect of Mu on the planar shape of the guanine nucleobase varies depending on the trapping sites. Non-planar characteristic of guanine base was observed when Mu is trapped at C4, C5, or C6 atoms. The guanine base retains its planar geometry when Mu is present at C2, C8, N3, N7, or O6 atoms. The results suggest that the most probable muon trapping sites are at the atoms with unsaturated bond. The Mu HFCC at the different sites ranges from -31.3 MHz to 366.3 MHz. The variation in the FCCC values at different trapping sites made it possible to experimentally differentiate the trapping sites in the guanine base. Based on the minimum total energy consideration, C8 is the most stable trapping site. The calculated value of the Mu Fermi contact coupling constant (FCCC) in the guanine nucleobase is in good agreement with the previous μSR data.

Moreover, the DFT method was employed to investigate the electronic structure and Mu hyperfine interaction of muon trapped near carbon atom labelled as '5' in cytosine nucleobase. Eighteen different basis sets in combination with B3LYP functional were examined in geometry optimization calculations on the muoniated radical. There are significant quantitative differences in the calculated total energy. The employment of basis set that does not include polarization function produces an optimized structure with high total energy. The 6-311++G(d,p) basis set yielded the lowest total energy as compared to other basis sets.

As a muon is trapped at a particular position in the studied system, it will covalently bond to the atom at the trapping site. In this investigation, the implanted μ+ was considered to capture an electron and formed a Mu. The bond length and bond order between Mu and atom at the trapping site can be obtained from computational investigation. Fig. 12 shows the bond length and the bond order between the Mu and the atom at the trapping site (Mu–C5) in cytosine nucleobase optimized structure calculated using the different types of basis sets. The bond order of Mu trapped at C5 atom is in the range of 0.841 to 0.862.

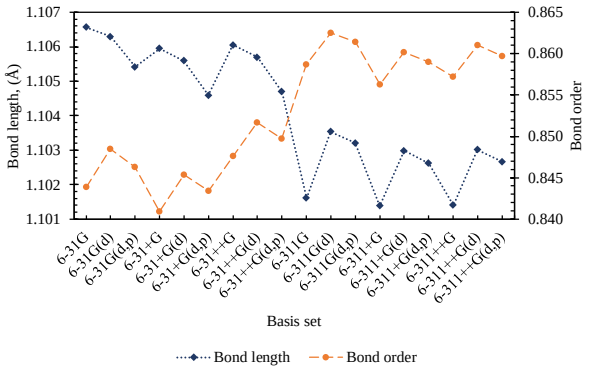

Fig. 12. Bond length and bond order.

For the Mu FCCC, all basis set produced Mu FCCC value that is similar or lower than the experimental value. The magnitude of the calculated Mu FCCC using different basis set ranges between 304 MHz to 341 MHz. The 6-31G basis set produced the Mu FCCC that is the closest to the experimental value.

Two computational methods were employed in this study to optimize the 12mer ssG oligomer, the PM6 semi-empirical method and the DFT method at the B3LYP/6-31G level. The purpose of geometry optimization is to obtain the optimal structure of 12mer ssG oligomer with minimum total energy. The atomic arrangement of the two optimized structures shows apparent differences. The optimized 12mer ssG oligomer obtained from the DFT method formed an s-shape structure while the PM6 method produced optimized geometry that is tree-like structure. The total energy of the PM6 structure is 21.5 eV higher as compared to the DFT structures.

v. Thiolated gold nanoclusters

DFT studies of the electronic and magnetic structures in these gold nanocluster systems have been performed using the Gaussian 16 software package. Fig. 13 and 14 show charge and spin density distributions in $[Au_{25}SR_{18}]^0$ system. The results demonstrate that this system features a high delocalization of the unpaired electron, where the magnitude is rather inhomogeneously distributed. This inhomogeneity is due to the distortions to the symmetry of the molecule corresponding to the Jahn Teller effects, which is common in the octahedral structures. Despite that, the distribution of spin densities is mainly centered on Au13 icosahedral core, as can be seen in Fig. 14.

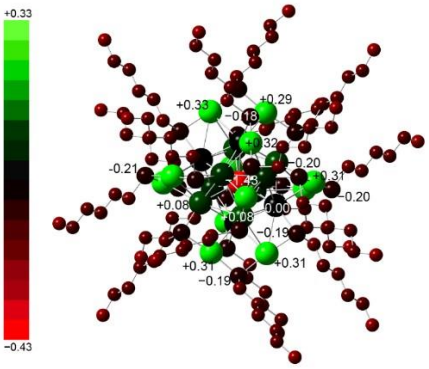

Fig. 13. Charge distribution of $(Au_{25}SR_{18})^0$ nanocluster using natural population analysis. The hydrogen atoms in the coordinating ligands were omitted for clarity. The color range is coded in accordance with the charge magnitudes, from the most negative magnitude, −1.43 to the most positive one, +0.33.

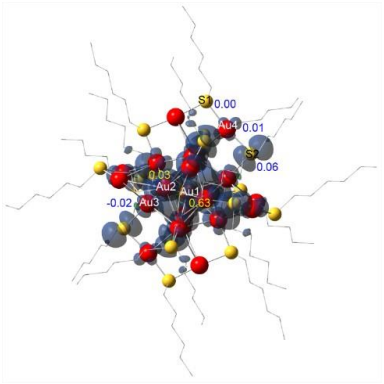

Fig. 14. Isosurfaces of $[Au_{25}SR_{18}]^0$ nanocluster spin density at the contour of 0.004 e–/au^3. The carbon and several other atoms were displayed in wire, and the hydrogen atoms in the coordinating ligands were omitted for clarity.

Fig. 15 shows the molecular electrostatic potential generated from the calculated total electron densities is used to locate the positive- and negatively charged electrostatic potentials in the systems. MEP can be a useful tool to predict the reactive sites for the electrophilic attack, where the positive muon serves as the electrophile. These sites are referred to as muon trapping sites. Muons will be

attracted to the locations with the high total electron densities and capture an electron from the system, forming an exotic atom called Mu. The highest electrostatic potentials in going from the most positive to the most negative regions are coded by blue, green, yellow, and red.

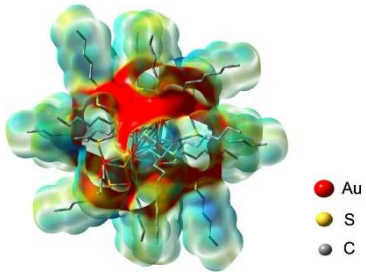

Fig. 15. Molecular electrostatic potential map generated from the calculated total electron density of $[Au_{25}(SR)_{18}]^0$ nanocluster. The isovalue used is 0.004 e−/a.u.^{3}.

Some of this research work have been presented in The Journal of Physical Society of Japan, entitled "Density Functional Theory Studies of Muon Stopping Sites and Hyperfine Interaction in $[Au_{25}(SR)_{18}]^0$ Nanocluster". The study covering the muon site calculations and associated hyperfine interactions in $Au_{25}SR_{18}$ with R = hexyl.

4. Conclusion

Currently, we have successfully carried out the computational work, which is the basis of our research efforts in studying the electronic and magnetic characteristics of these interesting target materials. The immense computing power of the HOKUSAI GreatWave supercomputer has provided an important contribution to our research efforts and enabled us to conduct a wide range of computationally intensive tasks in various materials. The computational results obtained assist us in understanding deeper the μSR experimental results. Some of the results obtained from our calculations have been successfully presented and published. Each of our subprojects has its own specific targets and objectives, which have been achieved. The accomplishment of every subproject is comprehensively concluded as follows:

i. Organic magnets

We have performed DFT calculations on the target systems by using Gaussian16 and ADF software. The muon stopping positions are successfully estimated in these organic magnets. These results are very valuable to make comparisons with μSR experimental results. The conclusions for the two subprojects are indicated as follow:

a. β'-X$[Pd(dmit)_2]_2$ X=$EtnMe_{4-n}$(P, Sb)

For the pure systems, some of the results have already been published in the Journal of the Physical Society of Japan (2018) and Materials Science Forum (2019). All computational work for these systems have already been completed and the objectives have been accomplished.

b. κ-$(BEDT\text{-}TTF)_2Cu[N(CN)_2]Cl$ and
κ-d8-$(BEDT\text{-}TTF)_2Cu[N(CN)_2]Br$

There are four possible muon sites are determined from DFT calculations which are C5, C20, S14 and S17 sites. The energy is the lowest at S17 position which can consider as the most stable site. From the values of HFCC computed using ADF software at the B3LYP level of theory for S17 and S14 are the closest to the observation from the experiment. The values at C5 and C20 using Gaussian software also are nearest to the one from the experiment.

ii. Organic superconductors, λ-$(STF)_2FeCl_4$

The result of the spin structure shows an AF ordering with the absolute value of localized magnetic moment of the spin in the STF dimer is 0.004 B which is much smaller as compared with a typical dimer Mott whose magnetic moment is ~0.1 B.

iii. High-Tc superconducting oxides

a. $YBa_2Cu_3O_6$

We have successfully estimated the muon site in YBCO and calculated the internal fields at the muon site. The expand of the spin in the real space due to the covalency effect is very important to explain the spin state in YBCO. The consistency of the experimental and calculation results of the internal fields have achieved by considering muon's perturbation to the system and zero-point vibration motion of the muon.

b. $La_{2-x}Sr_xCuO_4$

DFT + U method was successfully employed to investigate the electronic structure for both non-doped and 12.5 % Sr-doped case. For the non-doped case, we confirm that the hyperfine coupling contribution to the internal field is very small and in the order of less than 1%. Combination between distributed-spin model and the zero-point vibration motion of muon has successfully reproduced the experimental internal field with the accuracy reaching to 95 % for M1 and M3 position. For the 12.5 % Sr-doped case, metallic behavior is observed from the density of states.

iv. Single strand synthetic DNA model molecules

This study has identified all radical species that could result from the addition of Mu at the trapping sites in the nucleobase structure. This study provides an excellent overall understanding of the effect of Mu addition to the various trapping sites in the guanine base and the associated hyperfine properties. The addition of Mu at certain trapping sites provides a significant effect to the planar geometry of the nitrogenous base ring. The variation in the FCCC values at different trapping sites made it possible to experimentally differentiate the trapping sites in the guanine base.

Optimization calculations on the structure of muoniated cytosine nucleobase have been performed by using the DFT/B3LYP method with eighteen basis sets of Gaussian function. From this study we can conclude that, the accuracy of these calculations is dependent on the basis set completeness and of the correlation level.

The optimized structure of 12mer single strand guanine oligomer have been obtained. Based on the total energy, DFT method performed better than the semi-empirical method in obtaining the predicted optimized atomic arrangement of the system. Consequently, the optimized DFT structure was used to continue the study involve Mu.

v. Thiolated gold nanoclusters

From the charge and spin densities for the $[Au_{25}(SR)_{18}]$ pure system with 0 oxidation state, the system is found to have strong delocalized electron behavior with inhomogeneous distribution. This condition implies that there is a significant Jahn Teller effect in this system, which is well coincided with the previous studies. The spin densities show that the unpaired spin is mainly centered on the Au13 icosahedral core, which explains the magnetic origin of the system. From the calculations of the muonated system, there are three most stable muon stopping sites were determined, MAu10, MAu6, and MAu5 and the associated HFCC are −2.85 MHz, 62.63 MHz, and 3.56 MHz, respectively. The regions in the six staple motifs are unlikely to be muon stopping sites. The energy of the S sites in these regions is much higher than that for MAu10, and no local minima were found near the Au atoms in the staple motifs.

5. Schedule and prospect for the future

On the basis of our achievements in 2019, we plan to perform more complex calculations on our target systems and try to gain the following goals. We expect to continue and perform more complex calculations on our target systems. Therefore, more time is required, and it is of great importance for us to pursue our usage in HOKUSAI GreatWave supercomputer for FY2020.

i. Organic superconductors, λ-$(STF)_2FeCl_4$

The general future plan is to improve the current calculation before proceed with the calculation of the supercell 1 x 1 x 3 and including the muons. The next plan is to perform the dipole field calculation including the muons position and spin structure for several possible cases and compare with the internal field from μSR experiment data.

ii. High-Tc superconducting oxides

a. $YBa_2Cu_3O_6$

The numbers of muons that stop in each position directly proportional to the Fourier transform intensity. Our next plan is to clarify the probability of the muon stop at each muon site and compare to the Fourier transform intensity.

b. $La_{2-x}Sr_xCuO_4$

Detailed comparison concerning different concentration of Sr and also another cation atom of Ba will be considered on the next project. The general description of stripe on these two systems will also be discussed from the perspective of DFT+U calculation. Muon behavior on these two doped systems will be estimated using the similar method from the parent compound of La_2CuO_4.

iii. Single strand synthetic DNA model molecules

The optimized structure of 12mer single strand guanine (ssG) oligomer has been obtained. Details information on the muoniated 12mer ssG oligomer are needed. Thus, in the next fisical year, we would like to obtain the electronic structure of muoniated 12merssG oligomer and the associate hyperfine interactions. These calculations were then extended by using the other 12mer homogeneous single strand DNA (adenine, cytosine, and thymine).

iv. Thiolated gold nanoclusters, $[Au_{25}SR_{18}]$

For $Au_{25}SR_{18}$ with R = hexyl, we still have some calculations to be completed. The next targets for the gold nanocluster systems is we intend to study the effects of different type of ligands on the magnetic properties by substituting the sulfur groups or varying the alkyl groups. From this work, we are planning to submit two publications to the reputable academic journals.

Further description of our prospects is described in the research plan for 2020, which will be submitted to RIKEN after the submission of this report.

Usage Report for Fiscal Year 2019

Fiscal Year 2019 List of Publications Resulting from the Use of the supercomputer

[Paper accepted by a journal]

1. Ahmad, S. N. A., Sulaiman, S., Baseri, D. F. H., Ang, L. S., Yahaya, N. Z., Arsad, H., & Watanabe, I. (2020). Density Functional Theory Studies of Muon Stopping Sites and Hyperfine Interaction in $[Au_{25}(SR)_{18}]^0$ Nanocluster. Journal of the Physical Society of Japan, 89(1), 014301. (ISI Indexed)

[Conference Proceedings]

1. Ramli, I., Mohd-Tajudin, S.S., Ramadhan M.R., Mohamed-Ibrahim, M. I., Sulaiman, S., Sari, D.P., Kurniawan, B., Watanabe, I. Magnetic Properties of $YBa_2Cu_3O_6$ Studied by Density Functional Theory Calculation. In Materials Science Forum (Vol. 966, pp. 257-262). Trans Tech Publications Ltd.
2. Zaharim, W.N., Sulaiman, S., Abu Bakar, S.N., Ismail, N.E., Rozak, H., Watanabe, I. The Effects of Split Valence Basis Sets on Muon Hyperfine Interaction in Guanine Nucleobase and Nucleotides Structures. In Materials Science Forum (Vol. 966, pp. 222-228). Trans Tech Publications Ltd.
3. Ahmad S.N.A., Sulaiman, S., Ang, L.S., Watanabe, I. Effects of Polarization Function on the Spin Contamination and Distribution in ß'-$Me_4P[Pd(dmit)_2]$. In Materials Science Forum (Vol. 966, pp. 494-500). Trans Tech Publications Ltd.
4. M. R. Ramadhan, I. Ramli, M. D. Umar, S. Winarsih, A. Manaf, B. Kurniawan, M. I. Mohamed-Ibrahim, S. Sulaiman, I. Watanabe. Effects of the Supercell Size on the Muon Site Calculations of La_2CuO_4. Submitted to Key Engineering Materials Journal.In Materials Science Forum (Vol. 966, pp. 465-470). Trans Tech Publications Ltd.
5. Zaharim, W. N., Sulaiman, S., Abu Bakar, S. N., Ismail, N. E., Rozak, H., & Watanabe, I. First Principles Theory of Hyperfine Interactions in Guanine Nucleobase. ICMR 2019 – 8th International Conference on Multidisciplinary Research. (In review)
6. Zaharim, W. N., Tajudin, S. S., Sulaiman, S., Abu Bakar, S. N., Ismail, N. E., Rozak, H., & Watanabe, I. Basis Set Effects in Density Functional Theory of Guanine Muoniated Cytosine. Submitted to Key Engineering Materials Journal. (In Review)
7. Tajudin, S. S., Sulaiman, S., Ahmad, S. N. A., Zaharim, W. N., Hasan-Baseri, D. F., Ang, L. S., Yahaya, N. Z., Arsad, H., & Watanabe, I. Functional Effect in Density Functional Theory Calculation of $Au_{23}(SR)_{16}$ Nanocluster. Submitted to Key Engineering Materials Journal. (In Review)
8. Ramadhan, M. R., Ramli, I., Sari, D. P., Kurniawan, B., Manaf, A., Mohamed-Ibrahim, M. I., Sulaiman, S., Watanabe., I., Spin alignment Studies on the Muon-Site Determination in La2CuO4. Submitted to Key Engineering Materials Journal. (In review)

[Oral presentation]

1. Zaharim, W. N., Sulaiman, S., Abu Bakar, S. N., Ismail, N. E., Rozak, H., & Watanabe, I. (December, 2019). First Principles Theory of Hyperfine Interactions in Guanine Nucleobase. Oral presentations at Materials Research Meetings 2019. Yokohama, Japan.
2. Sari, D. P., Asih, R., Hiraki, K., Nakano, T., Nozue, Y., Hillier, A., Ishii, Y., Watanabe, I., (December, 2019). The admixture of an s-wave component into the d-wave superconducting gap symmetry in organic superconductor λ-$(BETS)_2GaCl_4$ studied by μSR. Oral presentation at Material Research *Meeting.* Yokohama, Japan.

3. Watanabe, I., Rozak, H., Zaharim, W. N., Sulaiman, S. (December, 2019) An Application of μSR in Biology, The Electron Transfer in DNA, Oral presentation at Materials Research Meetings 2019. Yokohama, Japan.
4. Zaharim, W. N., Sulaiman, S., Abu Bakar, S. N., Ismail, N. E., Rozak, H., & Watanabe, I. (August, 2019). First Principles Theory of Hyperfine Interactions in Guanine Nucleobase. Oral presentation at The 8th ICMR Conference 2018. Pulau Pinang, Malaysia.
5. Ramadhan, M. R., Ramli, I., Manaf, A., Kurniawan, B., Watanabe., I. (July, 2019). A Revisit to the Ordered State of Cu-Spins in La_2CuO_4 from the perspective of μSR and DFT. Oral presentation at the 5th International Symposium on Current Progress in Mathematics and Sciences 2019 (5th ISCPMS 2019), Depok, Indonesia.
6. Sulaiman, S., Zaharim, W. N., Abu Bakar, S. N., Ismail, N. E., Samian, M. R., Rozak, H., Watanabe, I., Mohamed-Ibrahim, M. I., & Kernain, D. (March, 2019). Observation and Simulation of 12mer Single Strand Guanine Oligomer. Oral presentation at International Conference on Ageing 2019. Pulau Pinang, Malaysia.
7. Sulaiman, S., Zaharim, W. N., Abu Bakar, S. N., Ismail, N. E., Samian, M. R., Rozak, H., Watanabe, I., Mohamed-Ibrahim, M. I., & Kernain, D. (March, 2019). DFT Studies on The Electronic Structures of 12mer Single Strand DNA Oligomers. Oral presentation at URICAS Symposium 2019. Pulau Pinang, Malaysia.
8. Watanabe, I., Rozak, H., Zaharim, W. N., Ismail, N. E., Abu Bakar, S. N., Miyazaki, I., Ichimura, K., Samian, M. R., Mohamed-Ibrahim, M. I., & Sulaiman, S. (March, 2019). The Study of Electrical Conductivity in 12-Mer Single-Stranded DNA by Muon-Spin Relaxation and Scanning Tunneling Microscopy. Oral presentation at URICAS Symposium 2019. Pulau Pinang, Malaysia.

[Poster presentation]

1. Zaharim, W. N., Sulaiman, S., Ahmad, S. N. A., Abu Bakar, S. N., Ismail, N. E., Rozak, H., & Watanabe, I. (December, 2019). The Effects of Split Valence Basis Sets on Muon Hyperfine Interaction in Guanine Nucleobase and Guanine Nucleotide Structures. Poster presentations at Materials Research Meetings 2019 (MRM 2019). Yokohama, Japan.
2. Ahmad, S. N. A., Sulaiman, S., Zaharim, W. N., Hasan-Baseri, D. F., Ang, L. S., Yahaya, N. Z., Arsad, H., & Watanabe, I. (December, 2019). Density Functional Theory Investigation of Muon Hyperfine Interactions in Au25SR18 Nanocluster. Poster presentations at Materials Research Meetings 2019 (MRM 2019). Yokohama, Japan.
3. Ramli, I., Ramadhan, M. R., Winarsih, S., Mohamed-Ibrahim, M. I., Sulaiman, S., Watanabe. I. (December, 2019). DFT and μSR Studies on $YBa_2Cu_3O_6$ and La_2CuO_4. Poster Presentation at the Materials Research Meeting 2019 (MRM 2019). Yokohama, Japan.
4. Sari, D. P., Minamidate, T., Matsunaga, N., Kawamoto, A., Ishii, Y., Watanabe, I. (December, 2019). μSR study of the Long-range Ordered State in Organic Antiferromagnet λ-$(STF)_2FeCl_4$: π-d spin interaction helps to increase T_N. Poster presentation at Material Research Meeting (MRM 2019). Yokohama, Japan.
5. Zaharim, W. N., Tajudin, S. S., Sulaiman, S., Abu Bakar, S. N., Ismail, N. E., Rozak, H., & Watanabe, I. (November, 2019). Basis Set Effects in Density Functional Theory of Guanine Muoniated Cytosine. Poster presentation at Padjadjaran International Physics Symposium. Bandung, Indonesia.
6. Tajudin, S. S., Sulaiman, S., Ahmad, S. N. A., Zaharim, W. N., Hasan-Baseri, D. F., Ang, L. S., Yahaya, N.

Z., Arsad, H., & Watanabe, I. (November, 2019). Functional Effect in Density Functional Theory Calculation of $Au_{23}(SR)_{16}$ Nanocluster. Poster presentation at Padjadjaran International Physics Symposium. Bandung, Indonesia.

7. Zaharim, W. N., Sulaiman, S., Abu Bakar, S. N., Ismail, N. E., Samian, M. R., Rozak, H., Watanabe, I., Mohamed-Ibrahim, M. I., & Kernain, D. (March, 2019). Simulation and Observation of 12mer Single Strand Guanine Oligomer. Poster presentation at URICAS Symposium 2019. Pulau Pinang, Malaysia.

[Others (Book, Press release, etc.)]

1. Ramadhan, M. R., Mohamed-Ibrahim, M. I., Sulaiman, S., & Watanabe., I. (2019). Quantum effects of muon on the electronic state of La_2CuO_4. RIKEN Accel. Prog. Rep. Peer Reviewed, 52, 173.